

# Water-Mediated Electrohydrogenation of CO<sub>2</sub> at Near-Equilibrium Potential by Carbon Nanotubes/Cerium Dioxide Nanohybrids

Giovanni Valenti,<sup>✉</sup> Michele Melchionna,<sup>✉</sup> Tiziano Montini, Alessandro Boni, Lucia Nasi, Emiliano Fonda, Alejandro Criado, Andrea Zitolo, Silvia Voci, Giovanni Bertoni, Marcella Bonchio,\* Paolo Fornasiero,\* Francesco Paolucci,\* and Maurizio Prato\*



Cite This: *ACS Appl. Energy Mater.* 2020, 3, 8509–8518



Read Online

ACCESS |



Metrics & More

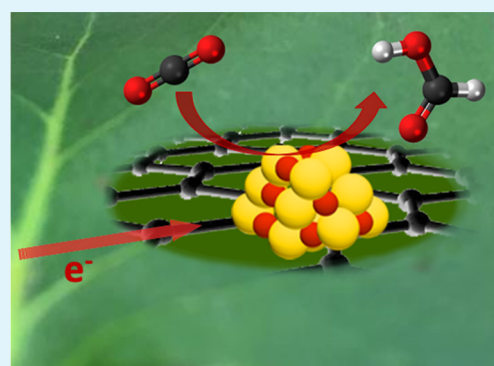


Article Recommendations



Supporting Information

**ABSTRACT:** The combination of multiwalled carbon nanotubes (MWCNTs) with undoped CeO<sub>2</sub> nanoparticles (NPs) is effective for the direct electrocatalytic reduction of CO<sub>2</sub> to formic acid (FA) at acidic pH (0.1 M HNO<sub>3</sub>), at overpotential as low as  $\eta = -0.02$  V (*vs* RHE) with Faradic efficiency (FE) up to 65%. *Ex situ* and *operando* evidence identifies nonstoichiometric Ce<sup>4+/3+</sup>O<sub>2-x</sub> reduced sites as essential for the selective CO<sub>2</sub> reduction reaction (CO<sub>2</sub>RR). The MWCNT-mediated electrochemical reduction of the CeO<sub>2</sub> NPs offers a definite advantage with respect to the generally adopted thermochemical cycles (800–1500 °C) or deep hydrogenation pretreatments, thus presenting an interesting perspective for the engineering of CeO<sub>2</sub> electrocatalysts.



**KEYWORDS:** carbon nanotubes, cerium oxide, carbon dioxide reduction, electrocatalytic hydrogenation, metal oxide electrocatalysts

## INTRODUCTION

The CO<sub>2</sub> reduction reaction (CO<sub>2</sub>RR) is being considered a two-way strategy for both environmental remediation and a carbon-zero circular economy.<sup>1</sup> Among all reduction products,<sup>2</sup> electrocatalytic CO<sub>2</sub> conversion into formic acid (FA) is particularly attractive, considering the application for direct formic acid fuel cells (DFAFCs) and the high volumetric hydrogen density of FA (4.4 wt %) and its low toxicity and liquid aggregation state, which make it a valuable hydrogen storage vector.<sup>3</sup> Indeed, FA is industrially produced by methanol carbonylation, using strong basic conditions and workup/extraction protocols.<sup>4</sup> Alternatively, selective hydrogenation of CO<sub>2</sub> is performed in one step but generally requires high temperature and high H<sub>2</sub>/CO<sub>2</sub> pressure conditions or supercritical CO<sub>2</sub> (scCO<sub>2</sub>) conditions in combination with noble-metal catalysts (Ir, Ru, Rh, Au).<sup>5</sup> Therefore, the direct electrohydrogenation of CO<sub>2</sub> to FA using water as the primary source of reactive hydrides offers a definite advantage for sustainable CO<sub>2</sub> processing. However, CO<sub>2</sub>RR in protic environments faces two major problems: the high overpotential<sup>6</sup> required for CO<sub>2</sub> activation and the current selectivity loss, due to the parallel hydrogen evolution reaction (HER) that generally occurs as a side reaction. Both issues can be addressed by a tailored design of the CO<sub>2</sub> reduction mechanism, which depends on the active sites of the electrocatalyst and on its surface properties.<sup>7,8</sup> A recent work has shown that Pd-based electrocatalysts can be tuned for CO<sub>2</sub>

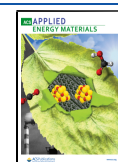
electrohydrogenation by introducing carbon-rich supports, conductive polymers, and Pt heterojunctions.<sup>9</sup> CO<sub>2</sub> electrohydrogenation is a mechanism whereby CO<sub>2</sub> is reduced by an electrochemically generated hydride surface on the catalyst surface. This strategy also allows the overstepping of possible CO formation as a byproduct, which for several transition metals is a serious problem, causing poisoning of the active species.<sup>10</sup> Following this approach, we have shown that the engineering of Pd@TiO<sub>2</sub> heterostructures on high-surface-area carbon nanostructures can leverage a selective CO<sub>2</sub> electrohydrogenation mechanism, at applied potential as low as  $-0.2$  V (*vs* RHE), with Faradic efficiency (FE) up to 95%.<sup>11</sup>

The lowering of CO<sub>2</sub>RR overpotential is fundamentally related to the stabilization of CO<sub>2</sub> reduction intermediates. Among redox-active oxides, ceria (CeO<sub>2</sub>) has been used to support noble metals for key catalytic applications including CO oxidation, CO<sub>2</sub> hydrogenation, water-gas shift reactions, and alcohol electro-oxidation in fuel cell applications.<sup>12–14</sup> The catalytic appeal of CeO<sub>2</sub> stems (i) from its relatively high natural abundance: Ce is among the most abundant metals on

**Received:** May 18, 2020

**Accepted:** August 19, 2020

**Published:** August 19, 2020



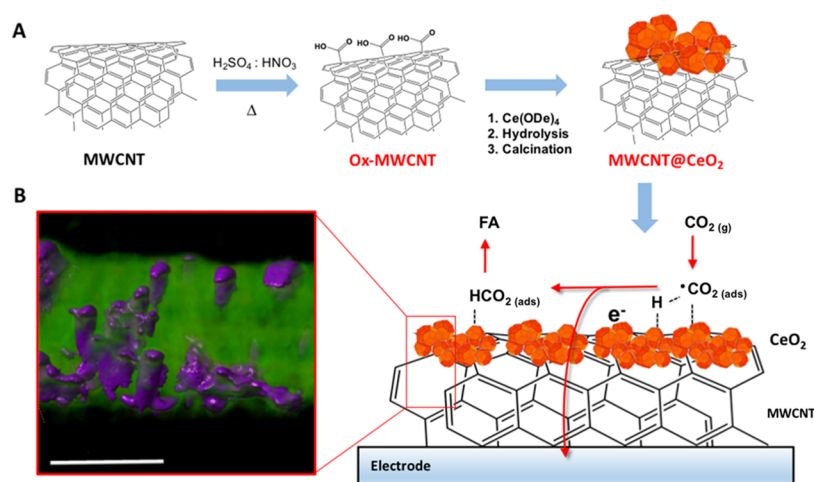


**Figure 1.** (A) Schematic of MWCNT@CeO<sub>2</sub> synthesis involving a first oxidation step of the MWCNT scaffolds, followed by decoration with CeO<sub>2</sub>-NPs, grown on the MWCNT surface by controlled hydrolysis of Ce<sup>4+</sup> tetrakis(decyloxy), Ce(ODe)<sub>4</sub>, and calcination at 250 °C. (B) Scanning transmission electron microscopy (STEM) tomographic reconstruction of MWCNT@CeO<sub>2</sub> (the region of high density corresponding to CeO<sub>2</sub> is rendered with a violet mesh) and a sketch of the possible mechanism of CO<sub>2</sub> hydrogenation to formic acid. Scale bar: 20 nm.

earth's crust, reaching 66.5 ppm, even more abundant than copper, 60 ppm<sup>15</sup> and (ii) from the reversible Ce<sup>4+/3+</sup> redox manifold, notably associated with the release or storage of oxygen atoms. The formation of oxygen vacancies in reduced CeO<sub>2</sub>, as also seen for other metal oxides,<sup>16</sup> is known to promote CO<sub>2</sub> binding and activation by reduced Ce<sup>3+</sup> sites with favorable electronic structures and surface and charge-transport properties.<sup>17</sup> In this regard, the impact of surface area/nanodimensions on the CeO<sub>2</sub> redox properties and on the oxygen defect formation is expected to be of central importance for tuning the energetics and the selectivity of the CO<sub>2</sub>RR process.<sup>17</sup> Finally, the use of more available elements in the construction of catalysts meets the current requirements for the implementation of sustainable schemes for chemical production. In particular, the replacement of precious metals is a modern endeavor in heterogeneous catalysis.<sup>18,19</sup>

Building on this concept, we report herein a novel CeO<sub>2</sub> nanocomposite (Figure 1) based on the combination of CeO<sub>2</sub> nanoparticles (NPs) with multiwalled carbon nanotubes (MWCNTs). The resulting MWCNT@CeO<sub>2</sub> electrocatalyst is effective for CO<sub>2</sub>RR to FA in acidic pH (0.1 M HNO<sub>3</sub>), at overpotential as low as  $\eta = -0.02$  V and with the overall FE > 65%, based on the simultaneous production of FA and H<sub>2</sub>, because all of the hydrogen generated at the low-overpotential regime comes from a <10% reversible FA dehydrogenation. While other metals including Pb, Cd, and Sn are known to produce FA with very good efficiencies, our composite's competitiveness capitalizes on the very low required overpotential (much lower than that of the mentioned metals) associated with excellent FE and on its low toxicity (Pb and Cd have considerable toxicity).<sup>20–22</sup> Notably, the state-of-the-art CO<sub>2</sub>RR with the comparably small overpotential is based on precious metals such as Pt, Au, Ag, and Pd, which, however, are associated with the tendency to yield different products such as CO.<sup>23,24</sup> On the other hand, cost-effective Cu catalysts required large overpotentials and typically lead to the formation of hydrocarbons.<sup>1,25</sup>

## EXPERIMENTAL SECTION

**Materials.** All glassware was dried in an oven set to a temperature of 80 °C for 24 h before use. All reagents were purchased from Sigma-

Aldrich and used without further purification. Phosphate buffer (PB) electrolytes were prepared readily before experiments from reagent-grade chemicals, mixing an appropriate amount of salts.

**Synthesis.** The pristine MWCNTs were first oxidized by a mixture of H<sub>2</sub>SO<sub>4</sub> and HNO<sub>3</sub>. In more detail, 150 mg of pristine MWCNTs (NanoAmor, 20–30 nm diameter, 0.5–2 μm length) was dispersed in a concentrated H<sub>2</sub>SO<sub>4</sub>/concentrated HNO<sub>3</sub> mixture (3:1 v/v, 100 mL) by sonication (6 h at 30–50 °C) and magnetic stirring (12 h at 50 °C). The suspension was washed six times by filtration [twice with water (250 mL), twice with NaOH (0.1 M, 250 mL), once with dimethylformamide (DMF) (250 mL), and once with tetrahydrofuran (THF) (250 mL)] to afford Ox-MWCNTs.

The MWCNTs@CeO<sub>2</sub> structures were prepared by a sol–gel method. The appropriate amount of Ce<sup>4+</sup>tetrakis(decyloxy) was dissolved in 25 mL of tetrahydrofuran (THF). The solution was then transferred to a sonicator, and an EtOH dispersion of Ox-MWCNTs was added. The mixture was kept under sonication for 30 min. A mixture of H<sub>2</sub>O (1 mL) and THF (10 mL) was added to ensure the complete hydrolysis of the alkoxide precursor, and the mixture was sonicated for an additional 15 min. The solid was then recovered by filtration and washed with THF three times and then dried at 120 °C overnight. The solid was finally calcined at 250 °C under static air. The reference material CeO<sub>2</sub> was prepared similarly but in the absence of Ox-MWCNTs.

**Electrochemistry.** Linear sweep voltammetry (LSV), cyclic voltammetry (CV), chronoamperometry (CA), and electrochemical impedance spectroscopy experiments were carried out in a three-electrode electrochemical cell using glassy carbon electrodes (CH Instruments, diameter 3 mm) as working electrodes. Electrochemical experiments were carried out in a home-made cell having a 5 mm diameter opening in front of the substrate electrodes. An O-ring ensures a perfect tightening of the assembly, thanks to connecting screws that fit directly into the body of the cell. A Biologic SP300 potentiostat was used as the workstation for all of the electrochemical experiments. All of the experiments were carried out in 0.5 M KHCO<sub>3</sub> or 0.1 M HNO<sub>3</sub> buffered solution freshly prepared readily before each experiment. The electrochemical cell was equipped with a platinum spiral counter electrode and a Ag/AgCl/KCl (3 M) reference electrode. All applied potentials were measured against a Ag/AgCl reference electrode (3.0 M KCl) and converted into the RHE reference scale [using  $E$  (vs RHE) =  $E_{app}$  (vs Ag/AgCl) + 0.210 V + 0.0591 V × pH, where  $E_{app}$  (vs Ag/AgCl) is the applied potential corrected for the Ohmic drop] or into overpotential [using  $\eta = E$  (vs RHE) –  $E^{\circ}_{[CO_2/FA]}$  (vs RHE), where  $E^{\circ}_{[CO_2/FA]}$  is the thermodynamic potential for the CO<sub>2</sub>/FA reaction ( $E^{\circ}_{[CO_2/FA]} = -0.2$  V vs RHE)]. All

of the solutions were thoroughly degassed with CO<sub>2</sub> at least 25 min before each experiment. The products formed during the electrochemical reduction of CO<sub>2</sub> were analyzed by online gas chromatography (GC) and ion chromatography (IC).

Thin films of the nanocomposites were prepared on the substrate working electrodes by deposition of the respective catalyst inks (methanol suspensions, 1.6 mg mL<sup>-1</sup>). The best performing films (Figure S1) combine good conductivity and an optimum catalyst loading (170 μg cm<sup>-2</sup>). Thin compact films were obtained with 5 μL aliquots subsequently added until a total deposited volume of 100 μL was reached. Those were then allowed to dry in the dark for at least 12 h, and the film thickness on the electrode surface, measured with a Tencor AlphaStep profilometer, was 8 ± 3 μm with a roughness of 3 ± 1 μm. The amount of catalysts deposited on the electrode surface was estimated to be 40 μg, with a mass contribution of CeO<sub>2</sub> of 65 wt %. In a similar way, compact films of nanocrystalline CeO<sub>2</sub> were prepared from analogous inks, by deposition of the same nominal amount of cerium dioxide onto the substrate electrodes.

**Faradic Efficiency (FE).** The Faradic efficiency for FA production at different *n* overpotentials is obtained by comparing the amount of the detected product with the charges exchanged by the nanocomposite electrode MWCNT@CeO<sub>2</sub> at the end of the electrolysis. The Faradic efficiency is defined as follows

$$(FE)_n(\%) = \frac{x_{\text{HCO}_2\text{H},n} \times F \times m}{Q_{\text{tot},n}} \quad (1)$$

where  $x_{\text{HCO}_2\text{H},n}$  denotes the moles of FA produced determined by IC, *F* is the Faraday constant, *m* is the number of electrons needed to produce one molecule of FA, and  $Q_{\text{tot},n}$  is the total charge integrated from chronoamperometry. Below are reported some chronoamperometries for MWCNT@CeO<sub>2</sub>, whose integration gives  $Q_{\text{tot},n}$ .

As pointed out in the main text, the so-obtained FE would never reach 100% value, due to the contribution of the Ce<sup>4+/3+</sup> reduction reaction in the overall charge,  $Q_{\text{tot},n}$ . One possibility arises from increasing the time scale of electrolysis or by subtracting the charge of Ce<sup>4+/3+</sup> reduction. The latter is not a straightforward approach because at this time is not clear if Ce<sup>3+</sup>, in addition to enhancing the local CO<sub>2</sub> concentration, also participates in the catalytic cycle. If Ce<sup>3+</sup> donates electrons to adsorbed CO<sub>2</sub>, it will become available again for further reduction, generating a positive feedback of charge that at the end would reduce the FE. Further investigation is thus needed to clarify the role of Ce<sup>3+</sup> and to determine the precise contribution of CeO<sub>2</sub> reduction to the overall charge and then to accurately determine the FE. Higher Faradic efficiencies may also be obtained, reducing surface inhomogeneities and maximizing the activity of CeO<sub>2</sub> to absorb and convert CO<sub>2</sub>.

**Turnover Frequency (TOF).** We estimate the TOF of the heterogeneous catalyst MWCNT@CeO<sub>2</sub> from the charge exchanged during electrolysis in a CO<sub>2</sub>-saturated electrolyte at a different overpotential, which is proportional to the amount of generated products: normalization for the quantity of the catalyst present is taken into account by dividing for the amount of electroactive material. The formula used to calculate the TOF for FA production with MWCNT@CeO<sub>2</sub> is the following

$$\text{TOF}_n(\text{h}^{-1}) = \frac{Q_{n,\text{red}}^{\text{CO}_2}(\text{C})}{Q_{\text{CeO}_2}(\text{C})} \times (FE)_n \times \frac{1}{\text{time}(\text{h})} \quad (2)$$

where  $Q_{n,\text{red}}^{\text{CO}_2}$  is the charge integrated from chronoamperometry experiments at the potential *n*;  $Q_{\text{CeO}_2}$  is the normalization factor for the amount of electroactive MWCNT@CeO<sub>2</sub>; time is the length of each electrolysis, usually 1 h long; and  $(FE)_n$  is the Faradic efficiency for FA production at each potential *n*. The obtained TOF<sub>*n*</sub> values reflect the opposite trends of FE, which increase, and integrated charges, which decrease, when reducing the overpotential. At low overpotentials, the absolute value of the charge is the lowest, but that charge is predominantly related to FA production, rather than

hydrogen evolution at high overpotential. This opposite trend results in TOF values around 100–200 h<sup>-1</sup> in the entire potential window.

## RESULTS AND DISCUSSION

The MWCNT scaffold boosts the electrocatalytic behavior of anchored CeO<sub>2</sub>-NPs for CO<sub>2</sub> electrohydrogenation by enhancing the surface area and electrical conductivity for charge transport (Figure 1B). Both features are instrumental to power the redox-active domains of CeO<sub>2</sub>-NPs, generating highly accessible, reduced Ce<sup>3+</sup>-hydridic sites and proximal oxygen defects that can bind and activate CO<sub>2</sub> while evolving to formate intermediates (HCO<sub>2</sub><sup>-</sup>, Figure 1B).<sup>26</sup> The morphology and electronic properties of carbon-based nanomaterials<sup>27</sup> are compelling features in the field of electrocatalysis.<sup>28,29</sup> In the present case, MWCNTs have a fundamental role in counteracting the insulating barrier of the oxide shell and leading to an efficient generation of nonstoichiometric (Ce<sup>4+/3+</sup>O<sub>2-x</sub>) with defected active sites on the NP surface that are essential for the selective CO<sub>2</sub>RR.<sup>17</sup> Noteworthy, the MWCNT-mediated electrochemical activation of the CeO<sub>2</sub> nanoislands stems as a breakthrough alternative to generally adopted high-temperature thermochemical cycles (800–1500 °C)<sup>30</sup> or deep hydrogenation pretreatments.<sup>31</sup>

It has been reported that carbon nanostructures (including MWCNTs) contain levels of transition-metal impurities such as Fe, Ni, Co, Mn, and Cu derived from the catalysts (or precursor) used in nanomaterial synthesis and that such metals could have a catalytic role.<sup>32,33</sup> For this reason, prior to the nanohybrid synthesis, the MWCNTs were washed several times with dilute HCl and HNO<sub>3</sub> to remove such impurities. To confirm the exclusion of trace metals, inductively coupled Plasma optical emission spectrometry (ICP-OES) was performed on the washed MWCNTs. None of the typical metals were found above the limit of detection of the instrument (10 ppb), with the exception of Ni, whose levels were, however, extremely low (<0.1 ppm) and likely due to carbon-shelled trace impurities. Based on the absence of CO<sub>2</sub> activation when ceria-free MWCNT are used as catalysts, the contribution of such low levels of Ni is expectedly negligible.

MWCNT@CeO<sub>2</sub> was synthesized by adapting a previously reported procedure (Figure 1A and the Experimental Section for synthetic details),<sup>34</sup> whereby oxidized MWCNTs are reacted in the presence of Ce<sup>4+</sup>tetrakis(decyloxyde), Ce(ODE)<sub>4</sub>, as an inorganic precursor. Oxidation of MWCNTs with HNO<sub>3</sub>/H<sub>2</sub>SO<sub>4</sub> provides a surface distribution of oxygenated groups (COOH, C–OH, and carbonyls), which are instrumental in securing the anchoring of Ce(ODE)<sub>4</sub>. Controlled hydrolysis of the Ce<sup>4+</sup> alkoxide precursor readily forms amorphous CeO<sub>2</sub> islands on the MWCNT surface. Finally, calcination at 250 °C leads to the crystallization of the CeO<sub>2</sub>-NPs (Figure 1A). The nominal weight percentage of MWCNT was chosen according to previous studies on CNT@CeO<sub>2</sub> structures to have the MWCNT not completely covered by CeO<sub>2</sub>, which would otherwise prevent an efficient contact between the conductive MWCNT and the supporting electrode, with the MWCNT insulated by the ceria shell.<sup>35</sup>

The relatively mild calcination temperature is expected not to introduce any significant amount of defects within the MWCNT surface, which may give a possible contribution to the catalysis. Raman analysis is in agreement with such a hypothesis. Thermogravimetric analysis (TGA) of the final MWCNT@CeO<sub>2</sub> material indicates that the CNT component

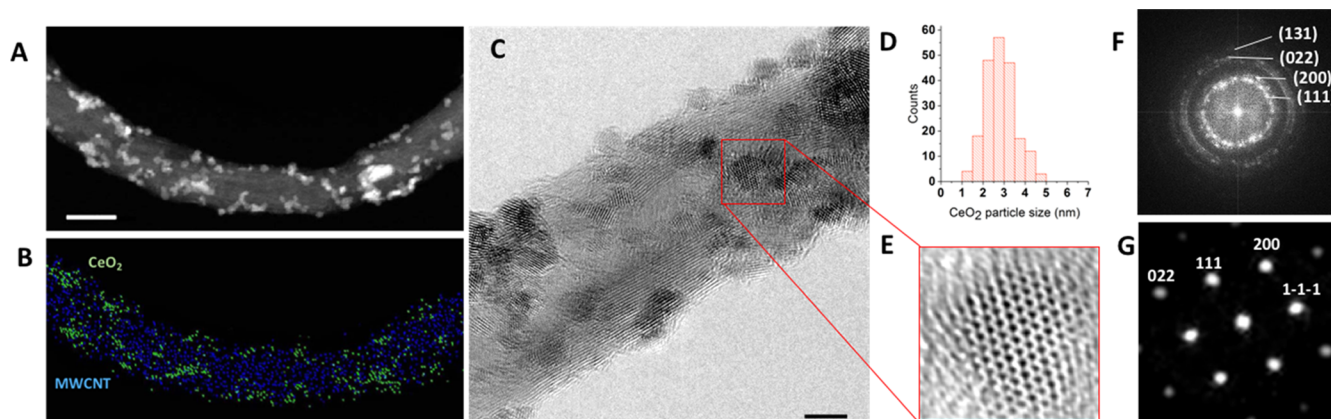


**Figure 2.** (A) STEM-HAADF of a typical MWCNT@CeO<sub>2</sub> and (B) corresponding EDX map highlighting the elemental distribution of C (blue) and Ce (green). Scale bar, 20 nm. (C) HRTEM of MWCNT@CeO<sub>2</sub>. Scale bar, 5 nm. The ring pattern in the fast Fourier transform (FFT) (F) can be indexed as the face-centered cubic structure of the crystalline CeO<sub>2</sub> nanoparticles. An enlarged image of a CeO<sub>2</sub> nanoparticle viewed along the (011) zone axis is shown in (E) with the corresponding FFT (G). (D) Particle size analysis of the MWCNT@CeO<sub>2</sub>.

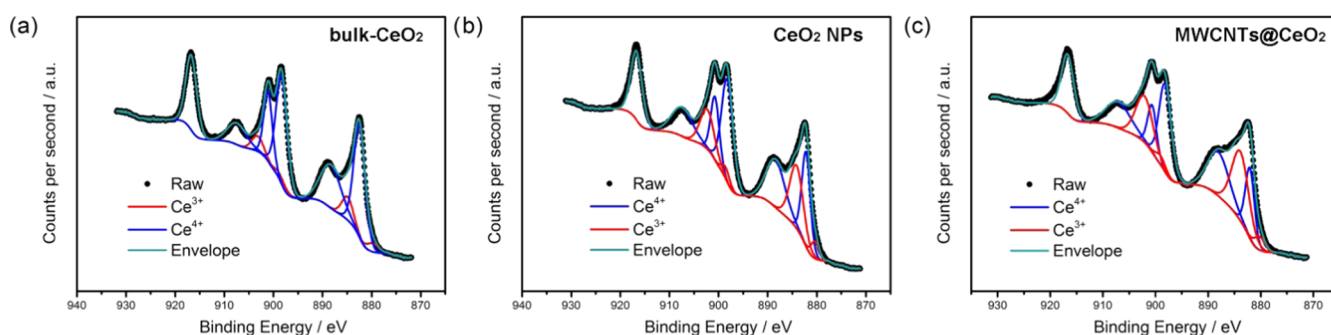


**Figure 3.** Fitted XPS spectrum of the Ce 3d core level of (a) bulk CeO<sub>2</sub>, (b) CeO<sub>2</sub> NPs, and (c) MWCNT@CeO<sub>2</sub>. XPS binding energies of individual components of the Ce 3d spectra for the different Ce-based samples.

**Table 1. Binding Energies of Individual Components of the Ce 3d Spectra of the Different Ce-Based Samples**

sample	Ce 3d <sub>5/2</sub> (eV)					Ce 3d <sub>3/2</sub> (eV)					[Ce <sup>3+</sup> ]
	v <sup>0</sup>	v	v'	v''	v'''	u <sup>0</sup>	u	u'	u''	u'''	
bulk-CeO <sub>2</sub>	879.72	882.49	884.89	888.32	898.35	898.4	901.07	903.19	907.46	916.7	0.11
CeO <sub>2</sub> NPs	880.37	882.19	884.13	888.4	898.2	898.5	900.71	902.28	907.44	916.7	0.25
MWCNT@CeO <sub>2</sub>	880.19	882.06	883.88	888.0	898.15	899.0	900.65	902.1	907.1	916.7	0.33

accounts for ~35 wt % (Figure S2), with the remaining 65% being ascribed to the CeO<sub>2</sub> NPs. This CeO<sub>2</sub> NP loading results in the best compromise between good conductivity and stability of the cathode. It must also be noted that the intimate contact with the CeO<sub>2</sub>-NPs leads to a remarkable decrease of the combustion temperature onset observed for the MWCNT@CeO<sub>2</sub> at ~350 °C in comparison with what is generally observed for the pristine CNTs (~600 °C). This behavior is consistent with the expected catalytic effect of CeO<sub>2</sub>-NPs, providing an excellent O buffer during oxidation.<sup>12</sup>

High-resolution and scanning transmission electron microscopy (HRTEM, STEM), in combination with high-angle annular dark-field imaging (STEM-HAADF), energy-dispersive X-ray spectroscopy (EDX), element mapping, and STEM tomography reconstruction, provides direct evidence for the material morphology and carbon-inorganic phase boundaries (Figures 1B, 2, S3 and S4). The inspection of the microscopy images confirms (i) the one-dimensional (1D) morphology resulting from the MWCNT templates with the diameter in the range 20–30 nm (Figure 2A–C), (ii) adhesion of

ultrasmall CeO<sub>2</sub> particles, showing a mean size of 2.8 ± 0.5 nm (Figure 2D), and (iii) the crystal lattice of the CeO<sub>2</sub> phase (face-centered cubic structure, Figure 2G), which is obtained after material calcination.

Raman spectra recorded for MWCNT@CeO<sub>2</sub> (Figure S5) show the typical pattern of graphitic materials, with D and G bands, respectively, at ~1330 and ~1580 cm<sup>-1</sup> and an intensity ratio of these bands of I<sub>D</sub>/I<sub>G</sub> ~ 1.27. The D band in carbon materials is associated with the presence of defects, which disrupt the graphitic network (which on the contrary gives rise to the G band). Hence, their ratio is typically used as a measure of the extent of defects on the CNT surface.<sup>36</sup> The low value of I<sub>D</sub>/I<sub>G</sub> (compared to that of the pristine MWCNT, 1.19) is therefore consistent with a mild modification of the nanocarbon scaffold properties with respect to the pristine MWCNTs, indicating the absence of additional defects generated during the calcination step. As expected, the appearance of a characteristic peak at 455 cm<sup>-1</sup> confirms the formation of a CeO<sub>2</sub> crystalline phase upon calcination (Figure S5, red and blue traces).<sup>37</sup>

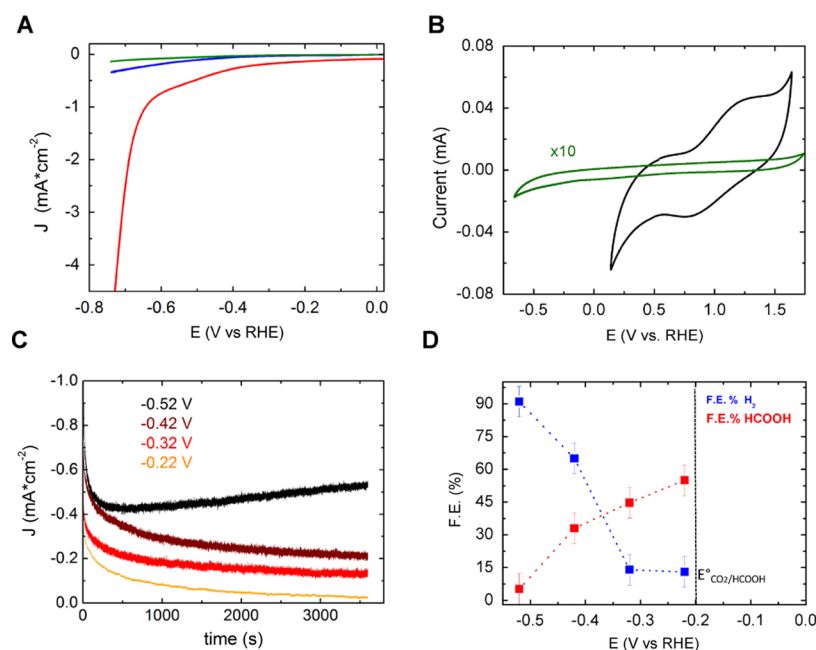


**Figure 4.** (A) LSV of the nanostructured catalyst  $\text{MWCNT@CeO}_2$  (red line), the bare GC electrode (blue line), and  $\text{CeO}_2$  NPs (green line) in a  $\text{CO}_2$ -saturated solution. Scan rate:  $2 \text{ mV s}^{-1}$ . Electrolyte:  $0.1 \text{ M HNO}_3$ . (B) CVs in  $0.1 \text{ M PB}$  for  $\text{MWCNT@CeO}_2$  (black curve) and  $\text{CeO}_2$  (green curve). Scan rate =  $50 \text{ mV s}^{-1}$ ,  $\text{pH} = 6.8$ . (C) CA for  $\text{MWCNT@CeO}_2$  at different overpotentials. Electrolyte:  $0.1 \text{ M HNO}_3$ . From orange to black,  $E = -0.22, -0.32, -0.42, -0.52 \text{ V (vs RHE)}$ . The integration of these CA gives the charge of  $\text{CO}_2$  reduction, then used for FE determination. (D) Faradic efficiency of  $\text{MWCNT@CeO}_2$  for FA (red) and  $\text{H}_2$  (blue) production as a function of the applied potentials. Electrolyte:  $0.1 \text{ M HNO}_3$ .

The MWCNT interface facilitates the  $\text{Ce}^{4+}$  reduction, thus increasing the  $\text{Ce}^{3+}$  content and the oxygen vacancy population in the  $\text{CeO}_2$  phase.<sup>12</sup> It is worth noting that the process of vacancy formation in ceria is very complex, with the coexistence of different situations of single and multiple vacancies.<sup>38</sup> However, important indications are gathered here *via* X-ray spectroscopy. To probe the initial  $\text{Ce}^{3+}$  fraction of the diverse materials, X-ray photoelectron spectroscopy (XPS) analysis was performed on bulk  $\text{CeO}_2$ ,  $\text{CeO}_2$  NPs, and the nanocomposite  $\text{MWCNT@CeO}_2$  (Figure 3 and Tables 1 and S1 and Figure S6). The relative  $\text{Ce}^{3+}$  content, which is associated with the formation of oxygen vacancies, was found to increase on downsizing the cerium oxide structure to the nanoscale and significantly enhanced upon the integration of the MWCNT component, with results in the series  $[\text{Ce}^{3+}] = 11, 25, \text{ and } 33$  (Figure 3).<sup>39</sup> This observation suggests that the MWCNT contact favors electron transport/injection and delocalization in the  $\text{CeO}_2$  layer, resulting in the accumulation of  $\text{Ce}^{3+}$  sites and oxygen vacancies, which turns out to be crucial for both  $\text{CO}_2$  binding and activation, and the formation of the reactive hydrides.<sup>40–42</sup>

Transmission electron microscopy and XPS analysis were also conducted on the postcatalysis material. From TEM and STEM-HAADF micrographs, it can be seen that the morphology and MWCNT-CeO<sub>2</sub> contact, as well as the crystallinity of the CeO<sub>2</sub> nanoparticles, remain unaltered as confirmed in the FFT of a selected area of the micrograph (Figure S7). XPS of the used catalyst confirms that no substantial change over the CeO<sub>2</sub> structure has occurred, with the  $[\text{Ce}^{3+}]$  in the aged  $\text{MWCNT@CeO}_2$  catalyst remaining comparable to the fresh one ( $0.33 \text{ vs } 0.27$ ); the slight decrease is presumably due to the required washing of the recovered catalyst before XPS analysis (Figure S8 and Table S2).

**$\text{CO}_2$  Electrocatalytic Reduction by  $\text{MWCNT@CeO}_2$ .** Thin films of  $\text{MWCNT@CeO}_2$  were deposited on a glassy

carbon electrode ( $\text{MWCNT@CeO}_2/\text{GC}$ ) and studied for the electrocatalytic reduction of  $\text{CO}_2$  to FA. The  $\text{CO}_2\text{RR}$  was evaluated by LSV, CV, and 1 h chronoamperometry (CA) under  $\text{CO}_2$ -saturated conditions. Products were analyzed by online GC directly connecting the headspace of the electrochemical cell to the sample loop of a GC, while FA was detected by analysis of the liquid phase by IC at the end of electrolysis (see Supporting Information for further details).

Noteworthy, LSV of  $\text{MWCNT@CeO}_2/\text{GC}$  performed in  $0.1 \text{ M HNO}_3$  under a  $\text{CO}_2$  atmosphere (red line, Figure 4A) shows a twofold feature: a steady current increase at applied potential as low as  $-0.2 \text{ V (vs RHE)}$ , followed by a sharp enhancement with the onset at  $-0.65 \text{ V (vs RHE)}$  (Figure 4A, red line). This latter is ascribed to the HER, occurring at unusually high overpotential on  $\text{MWCNT@CeO}_2/\text{GC}$ . Under such conditions, the Tafel analysis reveals a slope of  $140 \text{ mV dec}^{-1}$ , typical of the HER when the Volmer step, *i.e.*, the formation of the reactive intermediate  $\text{H}_{\text{ad}}$ , is the rate-determining step. In acids, the HER side reaction commonly occurs with electrocatalysts, such as Cu, Pt, or Pd, and at applied potentials as low as  $E \geq -0.1 \text{ V (vs RHE)}$ . The overpotential shift observed for the HER on  $\text{MWCNT@CeO}_2/\text{GC}$  leaves a broad selectivity window for the  $\text{CO}_2\text{RR}$ . Figure S9 shows the LSV and CV comparison with or without  $\text{CO}_2$  for the  $\text{MWCNT@CeO}_2$  catalyst, also compared with the profile for MWCNT alone. Indeed, the enhancement of the electrodic response at reduction potential  $> -0.4 \text{ V (vs RHE)}$ , Figure 4A red line) is definitely ascribed to  $\text{CO}_2$  saturation conditions when compared to under an Argon atmosphere (Figure S9, red line) and to MWCNT (Figure S9, black line). The electrocatalytic reduction of  $\text{CO}_2$  by  $\text{MWCNT@CeO}_2/\text{GC}$  is confirmed by the analysis of the electrolysis products that reveals the production of FA at potentials as low as  $-0.20 \text{ V (vs RHE)}$  (Figure 4C,D), *i.e.*, very close to the thermodynamic limit ( $-0.22 \text{ V vs RHE}$ ), for the  $\text{CO}_2/\text{FA}$

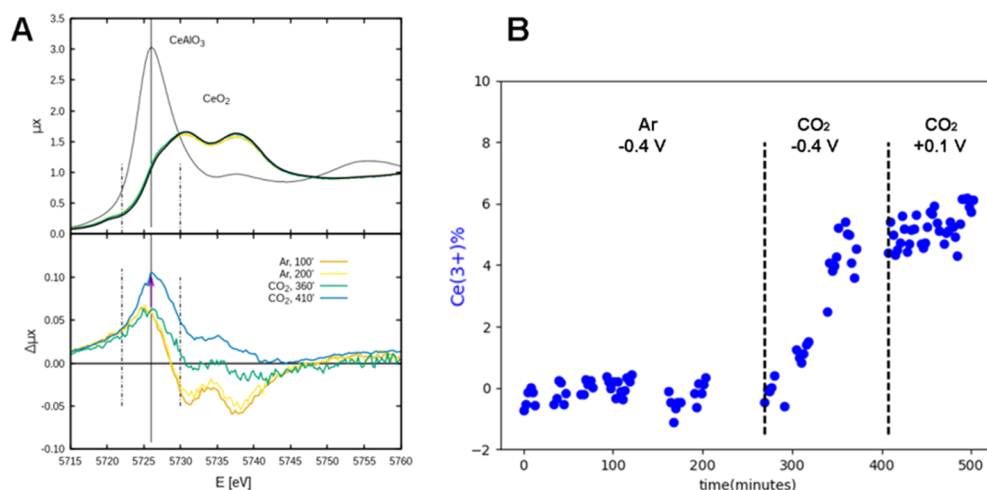


**Figure 5.** (A) Selected XANES spectra compared to those of two references (top) and  $\Delta\mu$  spectra vs OCP (bottom) of the same spectra. The dashed vertical arrows indicate the integration limits for evaluating the  $\text{Ce}^{3+}$  fraction reported in figure. (B) Evolution of the  $\text{Ce}^{3+}$  fraction before and after introducing  $\text{CO}_2$  in the cell.

conversion. A check of the electrolyte solution by  $^1\text{H}$  NMR did not show the formation of any other carbon products. The initial sudden current drop observed at all investigated fixed potentials (Figure 4C) is presumably due to the  $\text{Ce}^{4+}/\text{Ce}^{3+}$  reduction, after which the current remains rather stable. The slow progressive decline at longer times is likely due to a partial physical detachment of a fraction of the catalyst powder from the electrode, given that the ink deposition has not been fully optimized yet. Control experiments show that FA production is completely suppressed in the absence of  $\text{CO}_2$  (Figure S8), while any possible MWCNT-based origin of generated FA is excluded on the basis of isotope-labeling mass spectrometry experiments, using  $^{13}\text{CO}_2$ , which confirm the retention of the  $^{13}\text{C}$ -label in the produced FA (Figure S10), and on the comparison of the  $\text{CO}_2\text{RR}$  activity with the MWCNT (Figure S11).

Despite the tendency of  $\text{CeO}_2$  to slowly dissolve in a strong acidic environment,<sup>43</sup> we did not detect any presence of cerium in the postelectrolysis characterization under our conditions. While this could hint to a better stability of  $\text{CeO}_2$  when supported on MWCNT, a future more in-depth investigation will be required for a possible translation of our fundamental studies into a real application device. Recent density functional theory (DFT) calculations have shown the favorable binding of  $\text{CO}_2$  on partially reduced ceria (*i.e.*, in the presence of  $\text{Ce}^{3+}$  sites and oxygen vacancies).<sup>44,45</sup> The electrochemical  $\text{Ce}^{4+/3+}$  reduction turns out to be efficiently mediated by the MWCNT scaffold, at  $E \leq \sim 0.3$  V vs RHE.<sup>46</sup> Therefore, under  $\text{CO}_2\text{RR}$  conditions, generation of the non stoichiometric ceria sites ( $\text{Ce}^{4+/3+}\text{O}_{2-x}$ ) on  $\text{MWCNT@CeO}_2$  GC is responsible for  $\text{CO}_2$  activation and conversion into FA. Noteworthy, in the absence of MWCNTs, nanocrystalline  $\text{CeO}_2$  is not able to produce any significant Faradic current in the entire potential window explored (green line, Figure 4A,B). The possible formation of some cerium carboxylate species, favored in reduced ceria, cannot be ruled out. However, such species are not likely to take part in the catalysis due to their relatively good stability. In some cases, Ce-carbonate species have been identified during the  $\text{CO}_2\text{RR}$ , but they lead to the formation of CO, which is never detected during our  $\text{CO}_2\text{RR}$  experiments.<sup>30</sup>

*Operando* X-ray absorption spectroscopy (XAS) is recognized as a powerful technique for understanding the nature of  $\text{CO}_2\text{RR}$ -active sites<sup>47</sup> and here was used to gain further insights into the structural and chemical changes of  $\text{MWCNT@CeO}_2$  under an applied cathodic potential, either in the presence or in the absence of a  $\text{CO}_2$  atmosphere. To this end, the material thin film was deposited on a highly oriented pyrolytic graphite (HOPG) window and installed within the electrochemical cell (see Supporting Information for details). The X-ray absorption near-edge structure (XANES) spectra of  $\text{MWCNT@CeO}_2$  were recorded over time at the applied potential in the range  $-0.2$  to  $-0.7$  V, with a cathodic scan relative to the cell open-circuit potential (OCP = 0.540 V). XANES spectra were recorded initially under an Ar atmosphere (up to 280 min at  $-0.4$  V vs RHE) and then after saturating the electrolyte solution with  $\text{CO}_2$  by continuous  $\text{CO}_2$  bubbling (up to 410 min at  $-0.4$  V and cycled back at 0.1 V up to 500 min) and were then compared to those of the CNT-free material ( $\text{CeO}_2$  bulk,  $\text{CeO}_2$  NPs) and the  $\text{CeAlO}_3$  reference (Figure 5A and Table 2).<sup>48</sup> Although the content of  $\text{Ce}^{3+}$  cannot be precisely

**Table 2.** EXAFS Data Analysis Results

Ce–O	CN <sup>a</sup>	R(Å) <sup>b</sup>	$\sigma^2(10^{-3} \text{ \AA}^2)^c$
$\text{CeO}_2$	8.0(6)	2.34(1)	8(1)
nano- $\text{CeO}_2$	6.4(5)	2.33(1)	11(2)
MWCNT $\text{CeO}_2$			
(a) dry ink	6.2(6)	2.33(1)	13(2)
(b) $-0.7$ V $\text{CO}_2$	6.1(6)	2.35(1)	12(3)
(c) $-0.2$ V $\text{CO}_2$	6.1(5)	2.34(1)	9(2)

<sup>a</sup>CN = Coordination number. <sup>b</sup>R = Distance to the neighboring atom. <sup>c</sup> $\sigma^2$  = Mean-square disorder of the neighbor distance.

addressed from XANES spectra by a direct comparison or by linear combinations of standards (Figure 5A), the extended X-ray absorption fine structure (EXAFS) analysis indicates that both  $\text{CeO}_2$  NPs and  $\text{MWCNT@CeO}_2$  show (i) an average Ce–O bond length comparable within uncertainties to the bond length of  $\text{CeO}_2$  bulk and (ii) a decrease in the coordination number with respect to bulk  $\text{CeO}_2$  from 8 to 6 (Table 2). These data are consistent with an increased population of oxygen vacancies in the nanostructured samples,

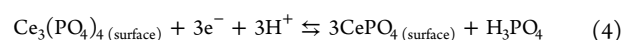
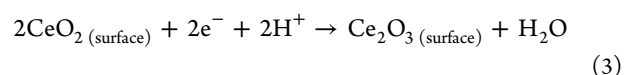
in close agreement with the XPS evidence, which reports much higher values and sensitivity related to surface-only fractions.<sup>49</sup>

To capture the structural and electronic changes of **MWCNT@CeO<sub>2</sub>** induced by the applied cathodic potential,<sup>50</sup> difference XANES spectra ( $\Delta\mu$ ) were calculated by subtracting the initial spectrum (at OCP = 0.540 V) from the *operando* spectrum recorded at increasing reduction potential and over time (Figure 4). Selected  $\Delta\mu$ -XANES spectra are reported in Figure 5, where a boosting effect for Ce<sup>3+</sup> production is apparent under a CO<sub>2</sub> atmosphere (Figure 5A). The evaluation of the  $\Delta\mu$  integral at around 5726 eV (integration from 5722 to 5730 eV as indicated by dashed lines and normalization by the  $\Delta\mu$  integral of CeAlO<sub>3</sub>, which is a Ce<sup>3+</sup> standard) provides the time-dependent fraction of Ce<sup>3+</sup>, showing a linear increase for the progressive reduction of **MWCNT@CeO<sub>2</sub>** under electrocatalytic CO<sub>2</sub> reduction, leveling off to a plateau value when the applied potential is cycled back to less reducing potentials (Figure 5B). The direct evidence of Ce<sup>3+</sup> accumulation monitored by *operando* XANES is consistent with the continuous H<sub>2</sub> formation in the explored potential range (Figure 4D and the Results and Discussion-section). H<sub>2</sub> is known to interact with CeO<sub>2</sub>-based materials, leading to progressive surface and bulk reduction under different conditions.<sup>51,52</sup> It has also been reported that the reduction is facilitated under applied voltages.<sup>53</sup> Here, the as-evolved H<sub>2</sub>, which originates from the dehydrogenation of the as-formed FA, can contribute to the further formation of Ce<sup>3+</sup> atoms, which occurs in parallel with the CO<sub>2</sub>RR and likely on different sites of the material, therefore being governed by independent kinetics. As a consequence, the growth of the Ce<sup>3+</sup> fraction linearly increases over 2 h of electrolysis, while it stops when the applied potential is increased to a regime (+0.1 V) where no CO<sub>2</sub> reduction occurs, confirming that the Ce<sup>3+</sup> generation is a consequence of FA formation. Because the steady Ce<sup>3+</sup> increase is not observed under an Ar atmosphere, we can conclude that the CeO<sub>2</sub> hydrogen-mediated reduction occurs at near-equilibrium overpotential as a result of the reversible FA dehydrogenation.

Although XPS and EXAFS results both confirm the more facile formation of oxygen vacancies within the nanohybrid, it must be stressed that the exact location of such vacancies cannot be univocally determined with only these two techniques. This is particularly true for ceria, given the high mobility of oxygen in this oxide, further enhanced by the applied electrochemical potential. Electrochemical impedance spectroscopy (EIS) and CV analysis were used to address the interaction of CO<sub>2</sub> molecules with the **MWCNT@CeO<sub>2</sub>**/GC. In particular, the double-layer capacitance ( $C_{dl}$ ) was found to increase significantly, confirming the adsorption of CO<sub>2</sub> on the electrode surface (Figure S12). In contrast, nanocrystalline CeO<sub>2</sub> films, in the absence of MWCNTs, yield much lower  $C_{dl}$  values that are not affected by the presence of CO<sub>2</sub> (Figure S13). Such a lower capacitance was attributed to a decrease of the electrochemically accessible CeO<sub>2</sub> surface, in turn associated with the much higher resistivity of the CeO<sub>2</sub> nanocrystals in the absence of MWCNTs. **MWCNT@CeO<sub>2</sub>** displayed similar  $C_{dl}$  values in a 0.5 M KHCO<sub>3</sub> buffered electrolyte, both in the presence and in the absence of CO<sub>2</sub>. This observation is consistent with the strong adsorption of carbonate on the CeO<sub>2</sub> surface.<sup>30</sup> We can thus postulate that the electrocatalytic mechanism leading to the CO<sub>2</sub> conversion into FA may occur *via* the formation of carbonate intermediates formed onto the ceria surface. To support the

favorable adsorption of CO<sub>2</sub> onto the nanocomposite, we carried out CO<sub>2</sub> chemisorption experiments on the nanocomposite and on the two reference materials CeO<sub>2</sub> and MWCNT. As shown in Figure S14, which reports the isotherms of the CO<sub>2</sub> chemisorption normalized by the material surface area, the quantity of CO<sub>2</sub> adsorbed per square meter is higher for the nanocomposite (Table S3) in comparison with either MWCNT or CeO<sub>2</sub>, corroborating the higher tendency of the catalyst to adsorb CO<sub>2</sub>.

**Electrochemical Analysis of the Mechanistic Features.** The peculiar surface activity of the substoichiometric mixed-valence Ce<sup>4+/3+</sup> oxide in the **MWCNT@CeO<sub>2</sub>** nanocomposite is clearly evident when operating in a PB solution (Figures 4B and S15). In this electrolyte, after reduction of Ce<sup>4+</sup> to Ce<sup>3+</sup> (eq 3), the formation of a surface CePO<sub>4</sub> species takes place (eq 4).<sup>46</sup> The latter reaction can be monitored by CV through the detection of a reversible peak with  $E_{1/2} = +1.1$  V (*vs* RHE, Figure S16).<sup>46</sup>



While the formation of CePO<sub>4</sub> leads to surface passivation and is detrimental in relation to the CO<sub>2</sub>RR (and therefore PB electrolytes should be avoided, Figure S16), monitoring of the process centered at  $E = +1.1$  V *vs* RHE provides a tool to estimate the amount of electroactive ceria, a necessary step for turnover frequency (TOF) determination (*vide infra*). It has to be noticed that the CePO<sub>4</sub> can be formed only in PB and not under the CO<sub>2</sub>RR experimental conditions. The integration of the corresponding CV peaks (Figures S17 and S15) reveals that ~20% of the total amount of CeO<sub>2</sub> deposited on the substrate electrode is reduced/oxidized electrochemically. Interestingly, the same redox process with  $E_{1/2} = +1.1$  V (*vs* RHE) is almost completely suppressed on films of nanocrystalline CeO<sub>2</sub> (Figure 4B). This difference highlights the essential role of MWCNTs in trafficking electrons to the surface of CeO<sub>2</sub>, thus promoting the electrocatalytic activity for CO<sub>2</sub>RR, otherwise inhibited in thicker and more insulating films. The long-term activity of **MWCNT@CeO<sub>2</sub>**/GC was assessed in 0.1 M HNO<sub>3</sub> by 1 h potential-controlled electrolysis in the range  $-0.22$  V <  $E_{\text{RHE}}$  <  $-0.52$  V. Stable current densities were obtained that increase proportionally at increasing applied potential (Figure 4C). CO<sub>2</sub> conversion into FA occurs at the near-equilibrium working potential (based on the thermodynamic value of  $-0.22$  V *vs* RHE) in close analogy with the natural formate dehydrogenase enzyme (FDH) bioelectrode.<sup>31</sup> In addition to FA, no other typical CO<sub>2</sub> reduction products, including CO, CH<sub>4</sub>, or CH<sub>3</sub>OH, were detected. However, the formation of H<sub>2</sub> is always observed in the explored potential range (Figure 4D). Interestingly, the inspection of the FA/H<sub>2</sub> selectivity, in terms of the relative FE %, shows an inversion cross-point at  $E < -0.4$  V (*vs* RHE, Figure 4D), with a quite high overpotential for the HER. This is indicative of a swapping of the electrocatalytic mechanism from the low- to high-overpotential regime. Control experiments have been performed that rule out H<sub>2</sub> generation in the absence of CO<sub>2</sub> at low overpotential ( $-0.52$  V <  $E_{\text{RHE}}$  <  $-0.22$  V) (Figure S18). This observation ascribes H<sub>2</sub> formation to FA dehydrogenation occurring under electrocatalytic conditions and accounting for *ca.* 10% FE. We might conclude that the CO<sub>2</sub>RR proceeds with an overall FE of *ca.* 65% at low

overpotential, while the HER takes over with FE up to ca. 90% at  $E < -0.6$  V (vs RHE). Importantly, MWCNT@CeO<sub>2</sub>|GC also displayed great chemical and mechanical stability with a linear increase of the FA generation and constant FE% in prolonged electrosynthesis (>16 h, Figure S19).

A dual electrocatalytic regime for MWCNT@CeO<sub>2</sub>|GC is also apparent, considering the Tafel plot analysis (Figure S20), where the slope of 140 mV dec<sup>-1</sup> is found at high overpotential, related to the HER, while a higher slope of 260 mV dec<sup>-1</sup> is found at low overpotential, related to the CO<sub>2</sub>RR mechanism. In this potential region, the occurrence of multiple and sequential chemical and electron transfer steps including the Ce<sup>4+/3+</sup> reduction, CO<sub>2</sub>/H<sup>+</sup> absorption and protonation equilibria, Ce<sup>3+</sup>-based hydride formation, and transfer to relevant intermediates, is expected to limit the kinetics, thus affecting the Tafel slope.<sup>54</sup> The high Tafel slope (>120 mV dec<sup>-1</sup>) and the selective FA generation at very low overpotential are consistent with a direct electrohydrogenation mechanism by MWCNT@CeO<sub>2</sub>.<sup>9</sup> The TOF for the FA production and H<sub>2</sub> evolution can be calculated from chronoamperometric experiments (see the Experimental Section) and turns out to be around 200 moles of FA for moles of CeO<sub>2</sub> for hours at -0.22 V (vs RHE, see eq 2 and Figure S19 and a production rate of 2 μmol h<sup>-1</sup> cm<sup>-2</sup>).

## CONCLUSIONS

The performance of MWCNT@CeO<sub>2</sub> for CO<sub>2</sub>/FA reversible electrohydrogenation in acidic electrolytes with FE up to 65% at near-equilibrium overpotential is rather unique, considering that it is ascribed to transition-metal-free active sites. A direct comparison with the state-of-the-art electrocatalysts for the CO<sub>2</sub>RR (Figure S21 and Table S5) ranks MWCNT@CeO<sub>2</sub> among the most promising systems reported to date in terms of the low overpotential combined with a wide selectivity window for the CO<sub>2</sub>RR. Hence, the concept of interfacing carbon nanostructures with CeO<sub>2</sub> holds great promise as further improvements of both the carbon nanoscaffolds and the electrode engineering, such as carbon fiber paper,<sup>55</sup> are expected to significantly enhance the production rate. Indeed, the use of high-surface-area carbon nanohorns (CNHs) decorated with CeO<sub>2</sub>-NPs (Figures S22 and S23) has been found to produce a 5-fold increase in the total charge after a chronoamperometric measurement under analogous electrocatalytic conditions (Figure S24). The optimization of CeO<sub>2</sub> loading might also contribute to further enhancements. Hence, the next generations of the catalyst, where the CeO<sub>2</sub> nanocarbon composite structure and composition will be further developed, will address limitations related to the moderate current densities, projecting ceria-based hybrid materials as a potential catalyst for industrial appeal.

## ASSOCIATED CONTENT

### Supporting Information

The Supporting Information is available free of charge at <https://pubs.acs.org/doi/10.1021/acsaem.0c01145>.

Experimental section on the product analysis; transmission electron microscopy; thermo-gravimetric analysis; Raman spectroscopy; X-ray photoelectron spectroscopy, and electrochemical characterization; TGA analysis, Raman spectrum; HRTEM; XPS; tafel slope analysis; and optimization of the material loading and stability (PDF)

## AUTHOR INFORMATION

### Corresponding Authors

**Marcella Bonchio** – ITM-CNR, Department of Chemical Sciences, University of Padova and Consortium INSTM, 35131 Padova, Italy; [orcid.org/0000-0002-7445-0296](https://orcid.org/0000-0002-7445-0296); Email: [marcella.bonchio@unipd.it](mailto:marcella.bonchio@unipd.it)

**Paolo Fornasiero** – Department of Chemical and Pharmaceutical Sciences, University of Trieste and Consortium INSTM, 34127 Trieste, Italy; ICCOM-CNR, University of Trieste, 34127 Trieste, Italy; [orcid.org/0000-0003-1082-9157](https://orcid.org/0000-0003-1082-9157); Email: [pfornasiero@units.it](mailto:pfornasiero@units.it)

**Francesco Paolucci** – Department of Chemistry “Giacomo Ciamician” and ICMATE-CNR Bologna Associate Unit, University of Bologna, 40126 Bologna, Italy; [orcid.org/0000-0003-4614-8740](https://orcid.org/0000-0003-4614-8740); Email: [francesco.paolucci@unibo.it](mailto:francesco.paolucci@unibo.it)

**Maurizio Prato** – Department of Chemical and Pharmaceutical Sciences, University of Trieste and Consortium INSTM, 34127 Trieste, Italy; Carbon Nanobiotechnology Laboratory, Center for Cooperative Research in Biomaterials (CIC biomaGUNE), Basque Research and Technology Alliance (BRTA), 20014 Donostia San Sebastián, Spain; Ikerbasque, Basque Foundation for Science, Bilbao 48013, Spain; [orcid.org/0000-0002-8869-8612](https://orcid.org/0000-0002-8869-8612); Email: [Pratoprato@units.it](mailto:Pratoprato@units.it)

### Authors

**Giovanni Valenti** – Department of Chemistry “Giacomo Ciamician”, University of Bologna, 40126 Bologna, Italy; [orcid.org/0000-0002-6223-2072](https://orcid.org/0000-0002-6223-2072)

**Michele Melchionna** – Department of Chemical and Pharmaceutical Sciences, University of Trieste and Consortium INSTM, 34127 Trieste, Italy; [orcid.org/0000-0001-9813-9753](https://orcid.org/0000-0001-9813-9753)

**Tiziano Montini** – Department of Chemical and Pharmaceutical Sciences, University of Trieste and Consortium INSTM, 34127 Trieste, Italy

**Alessandro Boni** – Department of Chemistry “Giacomo Ciamician”, University of Bologna, 40126 Bologna, Italy

**Lucia Nasi** – CNR-IMEM Institute, 43124 Parma, Italy

**Emiliano Fonda** – Synchrotron SOLEIL, L’Orme des Merisiers, 91192 Gif-sur-Yvette, France

**Alejandro Criado** – Carbon Nanobiotechnology Laboratory, Center for Cooperative Research in Biomaterials (CIC biomaGUNE), Basque Research and Technology Alliance (BRTA), 20014 Donostia San Sebastián, Spain

**Andrea Zitolo** – Synchrotron SOLEIL, L’Orme des Merisiers, 91192 Gif-sur-Yvette, France; [orcid.org/0000-0002-2187-6699](https://orcid.org/0000-0002-2187-6699)

**Silvia Voci** – Department of Chemistry “Giacomo Ciamician”, University of Bologna, 40126 Bologna, Italy

**Giovanni Bertoni** – CNR-IMEM Institute, 43124 Parma, Italy; CNR – Istituto Nanoscienze, 41125 Modena, Italy;

[orcid.org/0000-0001-6424-9102](https://orcid.org/0000-0001-6424-9102)

Complete contact information is available at: <https://pubs.acs.org/doi/10.1021/acsaem.0c01145>

### Author Contributions

<sup>✉</sup>G.V. and M.M. contributed equally.

### Notes

The authors declare no competing financial interest.

## ACKNOWLEDGMENTS

This work was supported by the Italian Ministero dell' Istruzione, Università e Ricerca (PRIN prot. 2017PBXP4), the H2020 - RIA-CE-NMBP-25 Program (Grant No. 862030), and Universities of Bologna and Trieste, INSTM; Dr. Matteo Crosera (University of Trieste) is acknowledged for the ICP-OES analysis. M.P., as the recipient of the AXA Chair, is grateful to the AXA Research Fund for financial support. This work was performed under the Maria de Maeztu Units of Excellence Program from the Spanish State Research Agency (Grant No. MDM-2017-0720).

## REFERENCES

(1) Voiry, D.; Shin, H. S.; Loh, K. P.; Chhowalla, M. Low-dimensional catalysts for hydrogen evolution and CO<sub>2</sub> reduction. *Nat. Rev. Chem.* **2018**, *2*, No. 0105.

(2) Kuhl, K. P.; Cave, E. R.; Abram, D. N.; Jaramillo, T. F. New insights into the electrochemical reduction of carbon dioxide on metallic copper surfaces. *Energy Environ. Sci.* **2012**, *5*, 7050–7059.

(3) Moret, S.; Dyson, P. J.; Laurency, G. Direct synthesis of formic acid from carbon dioxide by hydrogenation in acidic media. *Nat. Commun.* **2014**, *5*, No. 4017.

(4) Aresta, M.; Dibenedetto, A. Utilisation of CO<sub>2</sub> as a chemical feedstock: opportunities and challenges. *Dalton Trans.* **2007**, *28*, 2975–2992.

(5) Mellmann, D.; Sponholz, P.; Junge, H.; Beller, M. Formic acid as a hydrogen storage material – development of homogeneous catalysts for selective hydrogen release. *Chem. Soc. Rev.* **2016**, *45*, 3954–3988.

(6) Piernavieja-Hermida, M.; Lu, Z.; White, A.; Low, K.-B.; Wu, T.; Elam, J. W.; Wu, Z.; Lei, Y. Towards ALD thin film stabilized single-atom PdI catalysts. *Nanoscale* **2016**, *8*, 15348–15356.

(7) Hursán, D.; Janáky, C. Electrochemical Reduction of Carbon Dioxide on Nitrogen-Doped Carbons: Insights from Isotopic Labeling Studies. *ACS Energy Lett.* **2018**, *3*, 722–723.

(8) De Luna, P.; Quintero-Bermudez, R.; Dinh, C.-T.; Ross, M. B.; Bushuyev, O. S.; Todorović, P.; Regier, T.; Kelley, S. O.; Yang, P.; Sargent, E. H. Catalyst electro-deposition controls morphology and oxidation state for selective carbon dioxide reduction. *Nat. Catal.* **2018**, *1*, 103–110.

(9) Min, X.; Kanan, M. W. Pd-Catalyzed Electrohydrogenation of Carbon Dioxide to Formate: High Mass Activity at Low Overpotential and Identification of the Deactivation Pathway. *J. Am. Chem. Soc.* **2015**, *137*, 4701–4708.

(10) Daiyan, R.; Lu, X.; Tan, X.; Zhu, X.; Chen, R.; Smith, S. C.; Amal, R. Antipoisoning Nickel–Carbon Electrocatalyst for Practical Electrochemical CO<sub>2</sub> Reduction to CO. *ACS Appl. Energy Mater.* **2019**, *2*, 8002–8009.

(11) Melchionna, M.; Bracamonte, M. V.; Giuliani, A.; Nasi, L.; Montini, T.; Tavagnacco, C.; Bonchio, M.; Fornasiero, P.; Prato, M. Pd@TiO<sub>2</sub>/carbon nanohorn electrocatalysts: reversible CO<sub>2</sub> hydrogenation to formic acid. *Energy Environ. Sci.* **2018**, *11*, 1571–1580.

(12) Montini, T.; Melchionna, M.; Monai, M.; Fornasiero, P. Fundamentals and Catalytic Applications of CeO<sub>2</sub>-Based Materials. *Chem. Rev.* **2016**, *116*, 5987–6041.

(13) Chueh, W. C.; Falter, C.; Abbott, M.; Scipio, D.; Furler, P.; Haile, S. M.; Steinfeld, A. High-Flux Solar-Driven Thermochemical Dissociation of CO<sub>2</sub> and H<sub>2</sub>O Using Nonstoichiometric Ceria. *Science* **2010**, *330*, 1797–1801.

(14) Graciani, J.; Mudiyansele, K.; Xu, F.; Baber, A. E.; Evans, J.; Senanayake, S. D.; Stacchiola, D. J.; Liu, P.; Hrbek, J.; Sanz, J. F.; Rodriguez, J. A. Highly active copper-ceria and copper-ceria-titania catalysts for methanol synthesis from CO<sub>2</sub>. *Science* **2014**, *345*, 546–550.

(15) Yang, W.; Wang, X.; Song, S.; Zhang, H. Syntheses and Applications of Noble-Metal-free CeO<sub>2</sub>-Based Mixed-Oxide Nanocatalysts. *Chem* **2019**, *5*, 1743–1774.

(16) Daiyan, R.; Lovell, E. C.; Bedford, N. M.; Saputera, W. H.; Wu, K.-H.; Lim, S.; Horlyck, J.; Ng, Y. H.; Lu, X.; Amal, R. Modulating Activity through Defect Engineering of Tin Oxides for Electrochemical CO<sub>2</sub> Reduction. *Adv. Sci.* **2019**, *6*, No. 1900678.

(17) Gao, S.; Sun, Z. T.; Liu, W.; Jiao, X. C.; Zu, X. L.; Hu, Q. T.; Sun, Y. F.; Yao, T.; Zhang, W. H.; Wei, S. Q.; Xie, Y. Atomic layer confined vacancies for atomic-level insights into carbon dioxide electroreduction. *Nat. Commun.* **2017**, *8*, No. 14503.

(18) Monai, M.; Melchionna, M.; Fornasiero, P. Chapter One - From metal to metal-free catalysts: Routes to sustainable chemistry. In *Advances in Catalysis*, Song, C., Ed.; Academic Press, 2018; Vol. 63, pp 1–73.

(19) Daiyan, R.; Saputera, W. H.; Zhang, Q.; Lovell, E.; Lim, S.; Ng, Y. H.; Lu, X.; Amal, R. 3D Heterostructured Copper Electrode for Conversion of Carbon Dioxide to Alcohols at Low Overpotentials. *Adv. Sustainable Syst.* **2019**, *3*, No. 1800064.

(20) Huang, J.; Guo, X.; Huang, X.; Wang, L. Metal (Sn, Bi, Pb, Cd) in-situ anchored on mesoporous hollow kapok-tubes for outstanding electrocatalytic CO<sub>2</sub> reduction to formate. *Electrochim. Acta* **2019**, *325*, No. 134923.

(21) Chen, Z.; Fan, T.; Zhang, Y.-Q.; Xiao, J.; Gao, M.; Duan, N.; Zhang, J.; Li, J.; Liu, Q.; Yi, X.; Luo, J.-L. Wavy SnO<sub>2</sub> catalyzed simultaneous reinforcement of carbon dioxide adsorption and activation towards electrochemical conversion of CO<sub>2</sub> to HCOOH. *Appl. Catal., B* **2020**, *261*, No. 118243.

(22) Chen, Y.; Kanan, M. W. Tin Oxide Dependence of the CO<sub>2</sub> Reduction Efficiency on Tin Electrodes and Enhanced Activity for Tin/Tin Oxide Thin-Film Catalysts. *J. Am. Chem. Soc.* **2012**, *134*, 1986–1989.

(23) Hahn, C.; Abram, D. N.; Hansen, H. A.; Hatsukade, T.; Jackson, A.; Johnson, N. C.; Hellstern, T. R.; Kuhl, K. P.; Cave, E. R.; Feaster, J. T.; Jaramillo, T. F. Synthesis of thin film AuPd alloys and their investigation for electrocatalytic CO<sub>2</sub> reduction. *J. Mater. Chem. A* **2015**, *3*, 20185–20194.

(24) Back, S.; Yeom, M. S.; Jung, Y. Active Sites of Au and Ag Nanoparticle Catalysts for CO<sub>2</sub> Electroreduction to CO. *ACS Catal.* **2015**, *5*, 5089–5096.

(25) Reske, R.; Mistry, H.; Beharfarid, F.; Roldan Cuenya, B.; Strasser, P. Particle Size Effects in the Catalytic Electroreduction of CO<sub>2</sub> on Cu Nanoparticles. *J. Am. Chem. Soc.* **2014**, *136*, 6978–6986.

(26) Chen, S.; Cao, T.; Gao, Y.; Li, D.; Xiong, F.; Huang, W. Probing Surface Structures of CeO<sub>2</sub>, TiO<sub>2</sub>, and Cu<sub>2</sub>O Nanocrystals with CO and CO<sub>2</sub> Chemisorption. *J. Phys. Chem. C* **2016**, *120*, 21472–21485.

(27) Paolucci, D.; Marcaccio, M.; Bruno, C.; Paolucci, F.; Tagmatarchis, N.; Prato, M. Voltammetric quantum charging capacitance behaviour of functionalised carbon nanotubes in solution. *Electrochim. Acta* **2008**, *53*, 4059–4064.

(28) Valenti, G.; Boni, A.; Melchionna, M.; Cargnello, M.; Nasi, L.; Bertoni, G.; Gorte, R. J.; Marcaccio, M.; Rapino, S.; Bonchio, M.; Fornasiero, P.; Prato, M.; Paolucci, F. Co-axial heterostructures integrating palladium/titanium dioxide with carbon nanotubes for efficient electrocatalytic hydrogen evolution. *Nat. Commun.* **2016**, *7*, No. 13549.

(29) Toma, F. M.; Sartorel, A.; Iurlo, M.; Carraro, M.; Parisse, P.; Maccato, C.; Rapino, S.; Gonzalez, B. R.; Amenitsch, H.; Da Ros, T.; Casalis, L.; Goldoni, A.; Marcaccio, M.; Scorrano, G.; Scoles, G.; Paolucci, F.; Prato, M.; Bonchio, M. Efficient water oxidation at carbon nanotube–polyoxometalate electrocatalytic interfaces. *Nat. Chem.* **2010**, *2*, 826–831.

(30) Yu, Y.; Mao, B.; Geller, A.; Chang, R.; Gaskell, K.; Liu, Z.; Eichhorn, B. W. CO<sub>2</sub> activation and carbonate intermediates: an operando AP-XPS study of CO<sub>2</sub> electrolysis reactions on solid oxide electrochemical cells. *Phys. Chem. Chem. Phys.* **2014**, *16*, 11633–11639.

(31) Bassegoda, A.; Madden, C.; Wakerley, D. W.; Reisner, E.; Hirst, J. Reversible Interconversion of CO<sub>2</sub> and Formate by a Molybdenum-Containing Formate Dehydrogenase. *J. Am. Chem. Soc.* **2014**, *136*, 15473–15476.

- (32) Lum, Y.; Kwon, Y.; Lobaccaro, P.; Chen, L.; Clark, E. L.; Bell, A. T.; Ager, J. W. Trace Levels of Copper in Carbon Materials Show Significant Electrochemical CO<sub>2</sub> Reduction Activity. *ACS Catal.* **2016**, *6*, 202–209.
- (33) Mazánek, V.; Luxa, J.; Matějková, S.; Kučera, J.; Sedmidubský, D.; Pumera, M.; Sofer, Z. Ultrapure Graphene Is a Poor Electrocatalyst: Definitive Proof of the Key Role of Metallic Impurities in Graphene-Based Electrocatalysis. *ACS Nano* **2019**, *13*, 1574–1582.
- (34) Cargnello, M.; Grzelczak, M.; Rodriguez-Gonzalez, B.; Syrgiannis, Z.; Bakhtmutsky, K.; La Parola, V.; Liz-Marzan, L. M.; Gorte, R. J.; Prato, M.; Fornasiero, P. Multiwalled Carbon Nanotubes Drive the Activity of Metal@oxide Core-Shell Catalysts in Modular Nanocomposites. *J. Am. Chem. Soc.* **2012**, *134*, 11760–11766.
- (35) Beltram, A.; Melchionna, M.; Montini, T.; Nasi, L.; Gorte, R. J.; Prato, M.; Fornasiero, P. Improved activity and stability of Pd@CeO<sub>2</sub> core-shell catalysts hybridized with multi-walled carbon nanotubes in the water gas shift reaction. *Catal. Today* **2015**, *253*, 142–148.
- (36) Dumitru, A.; Mamlouk, M.; Scott, K. Effect of different chemical modification of carbon nanotubes for the oxygen reduction reaction in alkaline media. *Electrochim. Acta* **2014**, *135*, 428–438.
- (37) Spanier, J. E.; Robinson, R. D.; Zhang, F.; Chan, S.-W.; Herman, I. P. Size-dependent properties of CeO<sub>2</sub>-y nanoparticles as studied by Raman scattering. *Phys. Rev. B* **2001**, *64*, No. 245407.
- (38) Esch, F.; Fabris, S.; Zhou, L.; Montini, T.; Africh, C.; Fornasiero, P.; Comelli, G.; Rosei, R. Electron Localization Determines Defect Formation on Ceria Substrates. *Science* **2005**, *309*, 752–755.
- (39) López, J. M.; Gilbank, A. L.; García, T.; Solsona, B.; Agouram, S.; Torrente-Murciano, L. The prevalence of surface oxygen vacancies over the mobility of bulk oxygen in nanostructured ceria for the total toluene oxidation. *Appl. Catal., B* **2015**, *174–175*, 403–412.
- (40) Wu, Z.; Cheng, Y.; Tao, F.; Daemen, L.; Foo, G. S.; Nguyen, L.; Zhang, X.; Beste, A.; Ramirez-Cuesta, A. J. Direct Neutron Spectroscopy Observation of Cerium Hydride Species on a Cerium Oxide Catalyst. *J. Am. Chem. Soc.* **2017**, *139*, 9721–9727.
- (41) Yang, S.-C.; Su, W.-N.; Rick, J.; Lin, S. D.; Liu, J.-Y.; Pan, C.-J.; Lee, J.-F.; Hwang, B.-J. Oxygen Vacancy Engineering of Cerium Oxides for Carbon Dioxide Capture and Reduction. *ChemSusChem* **2013**, *6*, 1326–1329.
- (42) Aitbekova, A.; Goodman, E. D.; Wu, L.; Boubnov, A.; Hoffman, A. S.; Genc, A.; Cheng, H.; Casalena, L.; Bare, S. R.; Cargnello, M. Engineering of Ruthenium–Iron Oxide Colloidal Heterostructures: Improved Yields in CO<sub>2</sub> Hydrogenation to Hydrocarbons. *Angew. Chem., Int. Ed.* **2019**, *58*, 17451–17457.
- (43) Viro, M.; Chave, T.; Horlait, D.; Clavier, N.; Dacheux, N.; Ravoux, J.; Nikitenko, S. I. Catalytic dissolution of ceria under mild conditions. *J. Mater. Chem.* **2012**, *22*, 14734–14740.
- (44) Cheng, Z.; Sherman, B. J.; Lo, C. S. Carbon dioxide activation and dissociation on ceria (110): A density functional theory study. *J. Chem. Phys.* **2013**, *138*, No. 014702.
- (45) Albrecht, P. M.; Jiang, D.-e.; Mullins, D. R. CO<sub>2</sub> Adsorption As a Flat-Lying, Tridentate Carbonate on CeO<sub>2</sub>(100). *J. Phys. Chem. C* **2014**, *118*, 9042–9050.
- (46) Cummings, C. Y.; Stott, S. J.; Bonn e, M. J.; Edler, K. J.; King, P. M.; Mortimer, R. J.; Marken, F. Underpotential surface reduction of mesoporous CeO<sub>2</sub> nanoparticle films. *J. Solid State Electrochem.* **2008**, *12*, 1541–1548.
- (47) Daiyan, R.; Saputera, W. H.; Masood, H.; Leverett, J.; Lu, X.; Amal, R. A Disquisition on the Active Sites of Heterogeneous Catalysts for Electrochemical Reduction of CO<sub>2</sub> to Value-Added Chemicals and Fuel. *Adv. Energy Mater.* **2020**, *10*, No. 1902106.
- (48) Briois, V.; Lützenkirchen-Hecht, D.; Villain, F.; Fonda, E.; Belin, S.; Griesebock, B.; Frahm, R. Time-Resolved Study of the Oxidation of Ethanol by Cerium(IV) Using Combined Quick-XANES, UV–Vis, and Raman Spectroscopies. *J. Phys. Chem. A* **2005**, *109*, 320–329.
- (49) Zhang, F.; Wang, P.; Koberstein, J.; Khalid, S.; Chan, S.-W. Cerium oxidation state in ceria nanoparticles studied with X-ray photoelectron spectroscopy and absorption near edge spectroscopy. *Surf. Sci.* **2004**, *563*, 74–82.
- (50) Mijovilovich, A. Delta-mu XANES reveals the electronic structure of the adsorption of propene on gold nanoparticles. *RSC Adv.* **2014**, *4*, 12293–12297.
- (51) Perrichon, V.; Laachir, A.; Bergeret, G.; Fr e, R.; Tournayan, L.; Touret, O. Reduction of cerias with different textures by hydrogen and their reoxidation by oxygen. *J. Chem. Soc., Faraday Trans.* **1994**, *90*, 773–781.
- (52) Laachir, A.; Perrichon, V.; Badri, A.; Lamotte, J.; Catherine, E.; Lavalley, J. C.; El Fallah, J.; Hilaire, L.; Le Normand, F.; Qu em er e, E.; Sauvion, G. N.; Touret, O. Reduction of CeO<sub>2</sub> by hydrogen. Magnetic susceptibility and Fourier-transform infrared, ultraviolet and X-ray photoelectron spectroscopy measurements. *J. Chem. Soc., Faraday Trans.* **1991**, *87*, 1601–1609.
- (53) Gao, P.; Kang, Z.; Fu, W.; Wang, W.; Bai, X.; Wang, E. Electrically Driven Redox Process in Cerium Oxides. *J. Am. Chem. Soc.* **2010**, *132*, 4197–4201.
- (54) Kapalka, A.; F oti, G.; Comninellis, C. Determination of the Tafel slope for oxygen evolution on boron-doped diamond electrodes. *Electrochem. Commun.* **2008**, *10*, 607–610.
- (55) Burdyny, T.; Smith, W. A. CO<sub>2</sub> reduction on gas-diffusion electrodes and why catalytic performance must be assessed at commercially-relevant conditions. *Energy Environ. Sci.* **2019**, *12*, 1442–1453.